

The effects of large extra dimensions on associated $t\bar{t}h^0$ production at linear colliders *

Sun Hao², Zhang Ren-You², Zhou Pei-Jun², Ma Wen-Gan^{1,2}, Jiang Yi², Han Liang²

¹ CCAST (World Laboratory), P.O.Box 8730, Beijing 100080, P.R.China

² Department of Modern Physics, University of Science and Technology
of China (USTC), Hefei, Anhui 230027, P.R.China

Abstract

In the framework of the large extra dimensions (LED) model, the effects of LED on the processes $\gamma\gamma \rightarrow t\bar{t}h^0$ and $e^+e^- \rightarrow t\bar{t}h^0$ at future linear colliders are investigated in both polarized and unpolarized collision modes. The results show that the virtual Kaluza-Klein (KK) graviton exchange can significantly modify the standard model expectations for these processes with certain polarizations of initial states. The process $\gamma\gamma \rightarrow t\bar{t}h^0$ with $\sqrt{s} = 3.5 \text{ TeV}$ allows the effective scale Λ_T to be probed up to 7.8 and 8.6 TeV in the unpolarized and $P_\gamma = 0.9$, J=2 polarized $\gamma\gamma$ collision modes, respectively. For the $e^+e^- \rightarrow t\bar{t}h^0$ process with $\sqrt{s} = 3.5 \text{ TeV}$, the upper limits of Λ_T to be observed can be 6.7 and 7.0 TeV in the unpolarized and $P_{e^+} = 0.6$, $P_{e^-} = 0.8$, $-+$ polarized e^+e^- collision modes, respectively. We find the $\gamma\gamma \rightarrow t\bar{t}h^0$ channel in $J = 2$ polarized photon collision mode provides a possibility to improve the sensitivity to the graviton tower exchange.

PACS: 14.80.-j, 14.80.Cp, 04.50.+h

*Supported by National Natural Science Foundation of China.

I Introduction

In the late 1990's, a new solution to the hierarchy problem was proposed, which was accomplished by the presence of new large extra dimensions [1] [2], instead of low-energy supersymmetry [3] or technicolor [4]. Furthermore, the universe might have more than three spatial dimensions is not a brand new idea, and string theory has suggested that there could be up to seven additional spatial dimensions. In the large extra dimensions (LED) model, the relationship between extra dimensions' number n and LED compactification radius R is expressed by [1]

$$R \sim 10^{30/n-17} \text{cm} \times \left(\frac{1 \text{TeV}}{m_{\text{EW}}} \right). \quad (1.1)$$

The case of $n = 1$ is obviously ruled out, since it would modify Newton's law of gravity at solar-system distances. The case of $n = 2$ is also likely to be ruled out because of the results from the gravity experiments at submillimetre distance [5], and cosmological constraints from supernova cooling and distortion of cosmic diffuse gamma radiation as well [6]. As n increases from 2 to 10, $1/R$ increases from about 10^{-3} eV to about 1 GeV. Therefore, the standard model (SM) fields (gauge and matter fields) must be confined to the ordinary 4-dimensional space-time manifold, since the standard model has been tested up to $\sim 10^2$ GeV.

The large extra dimensions model becomes an attractive extension of the SM because of its possible testable consequences. As Arkani-Hamed, Dimopoulos, and Dvali [1] proposed, the SM particles exist in the usual $(3 + 1)$ -dimensional space, and graviton can propagate in a higher-dimensional space. Another manifestation of the large extra dimensions model is the existence of a Kaluza-Klein (KK) tower of

massive gravitons which can interact with the SM fields on the wall [7]. Experimental reviews on probing large extra dimensions are presented in Refs. [8] [9] [10], [11], [12] and [13].

Many papers have been concentrated on studying the LED effects on the processes at high energy colliders. The effective interactions of graviton and ordinary matter fields (fermions, gauge bosons and scalars) are presented in Ref. [14]. There are two classes of processes to probe LED effects: the real graviton emission processes and the virtual graviton exchange processes. For the second class of processes, any significant deviation from the SM prediction can be considered as the possible signal of the LED physics. In reference [15], the LED signatures of $\gamma + \cancel{E}$ and $jet + \cancel{E}$ as well as the virtual graviton exchange process $f\bar{f} \rightarrow \gamma\gamma$ at e^+e^- and $\mu^+\mu^-$ colliders, are investigated. Reference [16] studied the contributions of the graviton exchange in the process $\gamma\gamma \rightarrow W^+W^-$. It was found that the differential cross section as well as the polarization of W 's in the final state are quite sensitive to graviton exchange especially for certain initial photon polarizations. The exchange of Kaluza-Klein towers of massive gravitons in fermion pair production in e^+e^- annihilation and in Drell-Yan production are studied in Ref. [7]. It is concluded that future linear colliders and the LHC can exclude a string scale up to several TeV by measuring the LED effects in the $2 \rightarrow 2$ processes $e^+e^- \rightarrow f\bar{f}$, $q\bar{q} \rightarrow l^+l^-$, and $gg \rightarrow l^+l^-$. Recently, the studies of LED effects have been extended to three-body final states processes, such as $t\bar{t}h^0$, $h^0h^0Z^0$ and $h^0h^0\gamma$ productions at future e^+e^- and $\mu^+\mu^-$ colliders [17] [18] [19]. The results show that for $n = 3$, the processes of $e^+e^- \rightarrow h^0h^0Z^0$, $e^+e^- \rightarrow t\bar{t}h^0$ and $e^+e^- \rightarrow h^0h^0\gamma$ at a $\sqrt{s} = 3 \text{ TeV}$ linear collider,

can be used to put limits on the effective string scale M_s up to 6.6 TeV , 7.9 TeV and 7.4 TeV , respectively. In the intermediate Higgs boson mass region, the production mechanism with Higgs boson radiated from top-quark pair, is specially important. Due to the coupling strength of the top-quark-Higgs Yukawa coupling is proportional to the top-quark mass, the top quark Yukawa coupling g_{tth} is very large and the cross section of process $e^+e^- \rightarrow t\bar{t}h^0$ will be strongly enhanced. Therefore, the $e^+e^- \rightarrow t\bar{t}h^0$ process can be used to probe this coupling.

The GLC, NLC and TESLA e^+e^- linear colliders are designed with colliding energy from 300 GeV up to 1 TeV , while the CLIC at CERN is expected operating between $3 \sim 5\text{ TeV}$ colliding energy range. An e^+e^- LC can also be converted to a $\gamma\gamma$ collider. This is achieved by using Compton backscattered photons in the scattering of intense laser photons on an electron beam [20]. The resulting $\gamma\gamma$ center of mass system (CMS) energy is peaked at about $0.8\sqrt{s}$ for the appropriate choices of machine parameters. Generally e^+e^- collider has the advantage that the luminosity is higher than $\gamma\gamma$ collider (for example, $500\text{ fb}^{-1}/\text{year}$ of e^+e^- collider against $100\text{ fb}^{-1}/\text{year}$ of $\gamma\gamma$ one), but the polarization technique for photon is much simpler than positron. In Ref. [21], it is concluded that with careful handling of appropriate efficiency of b-tagging [22] [23] [24] and constraints of the W^\pm , t and h^0 masses, the backgrounds of signal $\gamma\gamma \rightarrow t\bar{t}h^0 \rightarrow b\bar{b}b\bar{b}W^+W^-$ process would be greatly reduced. Therefore, the $t\bar{t}h^0$ production at linear colliders in $\gamma\gamma$ collision mode would be another choice in testing the Yukawa coupling between Higgs boson and top quarks. At linear colliders (LC) $e^+e^- \rightarrow t\bar{t}h^0$ channel at high colliding energy can be used to test the existence of the virtual KK exchange[18]. But in both the

$e^+e^- \rightarrow t\bar{t}h^0$ and $\gamma\gamma \rightarrow t\bar{t}h^0$ processes, the role of proper initial particle polarization to improve the sensitivity to graviton tower exchange, hasn't been investigated until now. Therefore, the LED effects related to the polarizations of initial states in these processes would be worthwhile to study.

In this paper we study the indirect LED effects induced by the virtual KK graviton exchange in the processes $e^+e^- \rightarrow t\bar{t}h^0$ and $\gamma\gamma \rightarrow t\bar{t}h^0$, and emphasize the role of polarization of the initial states in improving the sensitivity to graviton exchange. In section 2 and 3, we present the calculations, numerical results and discussion for both processes. Finally, we give a short summary.

II Analytical Calculations

In this section, we present the analytical calculations of the two processes $\gamma\gamma \rightarrow t\bar{t}h^0$ and $e^+e^- \rightarrow t\bar{t}h^0$ involving KK graviton exchanges with different polarizations of incoming particles.

II.1 $\gamma\gamma \rightarrow t\bar{t}h^0$ process

At the tree-level, there are nine Feynman diagrams for the process $\gamma\gamma \rightarrow t\bar{t}h^0$. In Fig.1 we display only three of them which include KK graviton exchanges. The SM Feynman diagrams and their specific calculations in unpolarized photon collision mode can be found in Refs. [21] [27]. We denote this process as

$$\gamma(p_1, \lambda_1) + \gamma(p_2, \lambda_2) \rightarrow t(k_1, e_1) + \bar{t}(k_2, e_2) + h^0(k_3), \quad (2.1)$$

where λ_i and e_i are photon and top-quark/anti-top-quark polarizations, p_i ($i = 1, 2$) and k_i ($i = 1, 2, 3$) are the four-momenta of incoming photons and outgoing top-quark, anti-top-quark and Higgs boson, respectively. All these four-momenta satisfy the on-shell conditions: $p_1^2 = p_2^2 = 0$, $k_1^2 = k_2^2 = m_t^2$ and $k_3^2 = m_h^2$. The center-of-mass energy squared is denoted by $s = (p_1 + p_2)^2 = 2p_1 \cdot p_2$. The total helicity of the $\gamma\gamma$ system is $J = |\lambda_1 - \lambda_2|$.

In this paper, the amplitude of $\gamma\gamma \rightarrow t\bar{t}h^0$ process in the LED model is calculated under the de Donder gauge for simplicity. $F(k)_{AB,CD}^{(m)(m')}$, the graviton propagator under the de Donder gauge, can be expressed as [15]

$$F(k)_{AB,CD}^{(m)(m')} = \frac{i}{2} \frac{\delta_{m,m'}}{k^2 - M_m^2} \left(g_{AC}g_{BD} + g_{AD}g_{BC} - \frac{2}{D-2}g_{AB}g_{CD} \right), \quad (2.2)$$

where $D = 4+n$, M_m is the mass of m -th KK graviton and $(g_{AB}) = \text{diag}\{1, -1, \dots, -1\}$ is the metric tensor of the D -dimensional flat spacetime manifold. The amplitude for polarized initial photon beams can be divided into two parts:

$$\mathcal{M}(\lambda_1, \lambda_2) = \sum_{e_1, e_2} [\mathcal{M}^{SM}(\lambda_1, \lambda_2, e_1, e_2) + \mathcal{M}^{KK}(\lambda_1, \lambda_2, e_1, e_2)], \quad (2.3)$$

where \mathcal{M}^{SM} is the amplitude contributed by the SM-like diagrams, and

$$\begin{aligned} \mathcal{M}^{KK}(\lambda_1, \lambda_2, e_1, e_2) &= \mathcal{M}_1^{KK}(\lambda_1, \lambda_2, e_1, e_2) + \mathcal{M}_2^{KK}(\lambda_1, \lambda_2, e_1, e_2) \\ &\quad + \mathcal{M}_3^{KK}(\lambda_1, \lambda_2, e_1, e_2) \end{aligned} \quad (2.4)$$

is the amplitude related to all the three KK graviton exchanged diagrams presented in Fig.1. The summation is taken over the spins of final particles, since we do not consider the polarizations of top quarks. The analytic expression of

$\mathcal{M}_i^{KK}(\lambda_1, \lambda_2, e_1, e_2)$ ($i = 1, 2, 3$), which correspond to the Feynman diagrams in Figs.1(a), (b) and (c) respectively, are expressed explicitly as

$$\begin{aligned}
\mathcal{M}_1^{KK}(\lambda_1, \lambda_2, e_1, e_2) &= -\frac{1}{2}\bar{u}(k_1, e_1)g_{tth}v(k_2, e_1)\frac{D(s)}{(k_1 + k_2)^2 - m_h^2} \not{\epsilon}_\mu(p_1, \lambda_1) \not{\epsilon}_\nu(p_2, \lambda_2)C_{hhG}C_{\gamma\gamma G} \\
\mathcal{M}_2^{KK}(\lambda_1, \lambda_2, e_1, e_2) &= -\frac{1}{2}\bar{u}(k_1, e_1)g_{tth}\frac{\not{k}_1 + \not{k}_3 - m_t}{(k_1 + k_3)^2 - m_t^2} C_{ttG}v(k_2, e_2)D(s) \not{\epsilon}_\mu(p_1, \lambda_1) \not{\epsilon}_\nu(p_2, \lambda_2)C_{\gamma\gamma G} \\
\mathcal{M}_3^{KK}(\lambda_1, \lambda_2, e_1, e_2) &= -\frac{1}{2}\bar{u}(k_1, e_1)C_{ttG}\frac{\not{k}_2 + \not{k}_3 - m_t}{(k_2 + k_3)^2 - m_t^2} g_{tth}v(k_2, e_2)D(s) \\
&\quad \not{\epsilon}_\mu(p_1, \lambda_1) \not{\epsilon}_\nu(p_2, \lambda_2)C_{\gamma\gamma G} ,
\end{aligned} \tag{2.5}$$

where $g_{tth} = -igm_t/(2m_W)$, $C_{\gamma\gamma G}$, C_{hhG} and C_{ttG} are the relevant coupling constants given explicitly in Appendix, and $D(s)$ represents the summation of the KK excitation propagators

$$D(s) = \frac{1}{\bar{M}_{pl}^2} \sum_{m \in \mathbb{Z}^n} \frac{1}{s - M_m^2}. \tag{2.6}$$

In the LED theory, M_{pl} , the 4-dimensional Plank scale, is no longer a fundamental quantity, and is derived from the size R of extra dimension. The relationship between the ordinary reduced Planck scale $\bar{M}_{pl}(= \frac{M_{pl}}{\sqrt{8\pi}})$, the size of extra dimensions compactification radius R , extra dimensions number n and the fundamental Plank scale M_s is expressed as[15]

$$\bar{M}_{pl}^2 = R^n M_s^{n+2}. \tag{2.7}$$

As we know, the real part of the sum in Eq.(2.6) is divergent when n , the number of extra-dimensions, larger than 1. Since the LED model is an effective model, it is only valid below an effective energy scale. In phenomenology, the most plausible

assumption for $D(s)$ is [15]

$$D(s) = \lambda \frac{4\pi}{\Lambda_T^4}, \quad (2.8)$$

where λ is the sign of $D(s)$. This effective theory can be used only when \sqrt{s} smaller than the effective energy scale Λ_T . In the following numerical calculation, we fix λ to be 1.

Finally, the cross section for the polarized initial photon beams in the framework of the LED model reads

$$\sigma_{LED}^{pol.}(\lambda_1, \lambda_2) = \frac{N_c}{2|\vec{k}_1|\sqrt{s}} \int d\Phi_3 |\mathcal{M}(\lambda_1, \lambda_2)|^2, \quad (2.9)$$

and the phase-space hypercube element for three final particles process is defined as

$$d\Phi_3 = \left(\prod_{i=1}^3 \frac{d^3\vec{k}_i}{(2\pi)^3 2k_i^0} \right) (2\pi)^4 \delta\left(p_1 + p_2 - \sum_{j=1}^3 k_j\right). \quad (2.10)$$

Then the cross section for the unpolarized collision mode can be expressed as

$$\sigma_{LED}^{unpol.} = \frac{1}{4} \sum_{\lambda_1, \lambda_2} \sigma_{LED}^{pol.}(\lambda_1, \lambda_2). \quad (2.11)$$

II.2 $e^+e^- \rightarrow t\bar{t}h^0$ process

In Refs.[25][26], the process $e^+e^- \rightarrow t\bar{t}h^0$ can be used to probe the Yukawa coupling in the SM. The LED effects on the process $e^+e^- \rightarrow t\bar{t}h^0$ in unpolarized e^+e^- collision mode have been investigated by D. Choudhury, et al[18]. It was concluded that the measurement of $e^+e^- \rightarrow t\bar{t}h^0$ cross section with unpolarized colliding beams, will allow the effective string scale to be probed up to $M_s = 7.9 \text{ TeV}$ for $n = 3$ and $\sqrt{s} = 3 \text{ TeV}$. In this subsection we shall calculate the effects from additional

contributions of graviton exchange diagrams in the framework of the LED model on the cross sections of the $e^+e^- \rightarrow t\bar{t}h^0$ channel with different polarizations of initial states. The Feynman diagrams for the process $e^+e^- \rightarrow t\bar{t}h^0$ at the lowest level involving KK graviton exchanges are depicted in Fig.2. We denote this process as

$$e^+(p_1, \lambda_1) + e^-(p_2, \lambda_2) \rightarrow t(k_1, e_1) + \bar{t}(k_2, e_2) + h^0(k_3), \quad (2.12)$$

where λ_i and $e_i (i = 1, 2)$ are the positron/electron and top-quark/anti-top-quark helicities, separately. Analogous to the case in the $\gamma\gamma \rightarrow t\bar{t}h^0$ channel, we divide the amplitude into the SM-like part \mathcal{M}^{SM} and KK graviton exchange part \mathcal{M}^{KK} which can be easily obtained by using the Feynman rules presented in Ref.[14]. For the summation of the KK excitation propagators $D(s)$, we also use the assumption as shown in Eq.(2.8) and fix λ to be 1. The explicit analytical expressions corresponding to the three Feynman diagrams involving graviton exchange in Fig.2, $\mathcal{M}_i^{KK}(\lambda_1, \lambda_2, e_1, e_2)$ ($i = 1, 2, 3$), are presented as

$$\begin{aligned} \mathcal{M}_1^{KK}(\lambda_1, \lambda_2, e_1, e_2) &= -\frac{1}{2}\bar{u}(k_1, e_1)g_{tth}v(k_2, e_1)\frac{D(s)}{(k_1 + k_2)^2 - m_h^2} [\bar{v}(p_1)C_{eeGu}(p_2)]C_{hhG} \\ \mathcal{M}_2^{KK}(\lambda_1, \lambda_2, e_1, e_2) &= -\frac{1}{2}\bar{u}(k_1, e_1)g_{tth}\frac{k_1 + k_3 - m_t}{(k_1 + k_3)^2 - m_t^2} C_{ttG}v(k_2, e_2)D(s) [\bar{v}(p_1)C_{eeGu}(p_2)] \\ \mathcal{M}_3^{KK}(\lambda_1, \lambda_2, e_1, e_2) &= -\frac{1}{2}\bar{u}(k_1, e_1)C_{ttG}\frac{k_2 + k_3 - m_t}{(k_2 + k_3)^2 - m_t^2} g_{tth}v(k_2, e_2)D(s)[\bar{v}(p_1)C_{eeGu}(p_2)] \end{aligned} \quad (2.13)$$

where the explicit expressions of C_{ttG} and C_{eeG} can be found in Appendix. Finally, the cross section for the process $e^+e^- \rightarrow t\bar{t}h^0$ with polarized initial e^+e^- beams in the framework of the LED model can be calculated by using Eqs.(2.8-10).

III Numerical Results

In this section, we present some numerical results for both the $\gamma\gamma \rightarrow t\bar{t}h^0$ and $e^+e^- \rightarrow t\bar{t}h^0$ processes. In the numerical calculation, we take the input parameters as follows [28]

$$\begin{aligned} \alpha^{-1}(m_Z) &= 127.918, \quad m_W = 80.425 \text{ GeV}, \quad m_Z = 91.1876 \text{ GeV}, \quad m_t = 178.1 \text{ GeV} \\ \mathcal{L}_{e^+e^-} &= 500 \text{ fb}^{-1}, \quad \mathcal{L}_{\gamma\gamma} = 100 \text{ fb}^{-1}. \end{aligned} \quad (3.1)$$

We take the similar acceptance parameters with those in GLC[29] and assume

$$|\cos\theta_h| < 0.966 \quad \text{and} \quad |\cos\theta_t| < 0.95, \quad (3.2)$$

where θ_h and θ_t are the angles between h^0 , top quark and the incoming e^- and one of the colliding photon beams, respectively.

III.1 $\gamma\gamma \rightarrow t\bar{t}h^0$

There are five kinds of polarization collision modes for the $\gamma\gamma \rightarrow t\bar{t}h^0$ channel. They are $+-$, $-+$, $++$, $--$ and unpolarized collision modes, separately (e.g., the notation of $+-$ represents the helicities of the two initial photons being $\lambda_1 = +1$ and $\lambda_2 = -1$). In Fig.3(a), we present the cross sections of $\gamma\gamma \rightarrow t\bar{t}h^0$ as a function of the c.m.s. energy \sqrt{s} in different kinds of collision modes. Here we take $m_h = 115 \text{ GeV}$ and $\Lambda_T = 3.5 \text{ TeV}$. Since the cross sections of the $+-$ and $-+$ photon polarizations ($J=2$) are equal, and same is true for the cross sections of the $++$ and $--$ photon polarizations ($J=0$), we only depict the results in the $+-$, $++$ and unpolarized photon collision modes, which are represented by the dashed, dotted

and solid curves, respectively. As the figure shows that in the energy region where $\sqrt{s} < 0.7TeV$, the two curves of the SM and LED model for unpolarized or $+-$ polarized photon collision are overlapped, but when the colliding energy goes up from $0.7TeV$ to $3.5TeV$, each curve branches off into two curves. The lower and upper curves represent the SM and LED results, respectively. In Fig.3(a), we see that both the SM and LED results for $++$ collision mode are shown by the same dotted curve, that means the cross sections in both models in $++$ collision mode are almost the same. In Fig.3(b), we depict the cross sections and the ratio between the cross sections in the $+-$ and $++$ collision modes, where the ratio Δ is defined as

$$\Delta = \sigma_{+-}/\sigma_{++}. \quad (3.3)$$

It is obviously that the $\gamma\gamma \rightarrow t\bar{t}h^0$ channel in the J=2 polarized photon collision mode provides the possibility to improve the sensitivity in probing the LED effects. We will focus on this kind of polarization collision channel in the following calculation.

Fig.4 exhibits the cross sections for the process $\gamma\gamma \rightarrow t\bar{t}h^0$ as the functions of c.m.s. energy \sqrt{s} for different values of Λ_T and m_h . The solid curves represent the SM results, the dashed, dotted, dash-dotted, dash-dotted-dotted and short dashed curves represent the cross sections for $\Lambda_T = 2.5, 3.5, 4.5, 5.5$ and 6.5 TeV, respectively. In the figures of Fig.4, we take m_h to be 115, 150 and 200 GeV for comparison respectively. The Figs.4(a), (c) and (e) are for unpolarized collision mode and Figs.4(b), (d) and (f) are corresponding to the $+-$ (J=2) polarized collision mode. Again we can see that the virtual KK graviton exchange can modify the cross section

of the $\gamma\gamma \rightarrow t\bar{t}h^0$ process significantly from its SM prediction in both J=2 polarized and unpolarized photon collision modes. As we expected that when colliding energy \sqrt{s} is large enough, there is an obvious enhancement for σ_{LED} , while the σ_{SM} goes down slowly with the increment of \sqrt{s} .

In Fig.5, we present the dependence of the cross section of the $\gamma\gamma \rightarrow t\bar{t}h^0$ process in both unpolarized and J=2, $P_\gamma(= \frac{N_+-N_-}{N_++N_-}) = 0.9$ collision modes, on the parameter Λ_T with $m_h = 115, 150$ and 200 GeV, respectively. For comparison in different colliding energies, we take the $\gamma\gamma$ colliding energy \sqrt{s} to be 1, 2 and 3 TeV, which are represented by solid, dashed and dotted curves, respectively. For each fixed values of \sqrt{s} and m_h , the cross section σ_{LED} goes down and approaches to its corresponding SM result(σ_{SM}) as the increment of Λ_T . This dependence of the cross section for the $\gamma\gamma \rightarrow t\bar{t}h^0$ process on effective scale Λ_T typically reflects the relation of $\mathcal{M}^{KK} \propto \Lambda_T^{-4}$, and the $t\bar{t}h^0$ associated production process in J=2, $P_\gamma = 0.9$ polarized collision mode improves obviously the sensitivity to the LED effective scale Λ_T .

As demonstrated in above figures, the virtual KK graviton exchange in both unpolarized and $J = 2, P_\gamma = 0.9$ polarized photon collision modes can obviously modify the cross section of the $\gamma\gamma \rightarrow t\bar{t}h^0$ process from its SM value, if the large extra dimensions really exist. Since the large extra dimensions can be probed only when the deviation of the cross section within the framework of the LED model from its SM value, $\Delta\sigma$, is large enough, we assume that the LED effect can and can not be observed, only if

$$\Delta\sigma = \sigma_{LED} - \sigma_{SM} \geq \frac{5\sqrt{\sigma_{LED}\mathcal{L}}}{\mathcal{L}}, \quad (3.4)$$

and

$$\Delta\sigma = \sigma_{LED} - \sigma_{SM} \leq \frac{3\sqrt{\sigma_{LED}\mathcal{L}}}{\mathcal{L}}, \quad (3.5)$$

respectively.

In Figs.6(a),(b) and (c), we show the regions in $\sqrt{s} - \Lambda_T$ parameter space for the process $\gamma\gamma \rightarrow t\bar{t}h^0$ with unpolarized incoming photons, where the LED effect can and cannot be observed according to above criteria, for $m_h = 115, 150$ and 200 GeV, respectively. Here we take the integrated luminosity for $\gamma\gamma$ collider as $\mathcal{L} = \mathcal{L}_{\gamma\gamma} = 100fb^{-1}$. The underside grey region is excluded by the unitarity bounds.

In Table 1, we present the regions of 3σ exclusion limits and corresponding 5σ observation limits for the $\gamma\gamma \rightarrow t\bar{t}h^0$ process in both unpolarized and J=2 polarized collision modes with $m_h = 115, 150, 200$ GeV and some typical \sqrt{s} values of LC, respectively. For the J=2 polarized photon collision mode, the beam polarization P_γ is set to be 0.9. From this table we can find that the process $\gamma\gamma \rightarrow t\bar{t}h^0$ in the $P_\gamma=0.9$, J=2(i.e., $+-$, $-+$ photon polarizations) polarized photon collision mode can be used to improve the sensitivity of probing the LED model effects. For $\sqrt{s}=3.5$ TeV and $m_h=115$ GeV, the observation limits on Λ_T can be probed up to 8.6 TeV and the exclusion limits on Λ_T can be probed up to 9.8 TeV.

Fig.7 exhibits the \sqrt{s} dependence of relative discrepancy between the cross sections in the LED model and SM for process $\gamma\gamma \rightarrow t\bar{t}h^0$ in unpolarized and $J = 2$, $P_\gamma = 0.9$ polarized collision modes respectively, where the relative discrepancy δ is defined as

$$\delta = \frac{\sigma_{LED} - \sigma_{SM}}{\sigma_{SM}}. \quad (3.6)$$

$m_h = 115[\text{GeV}]$	Λ_T [GeV]	
\sqrt{s}	<i>unpol.</i>	$J = 2$ <i>pol.</i>
[TeV]	3σ , 5σ	3σ , 5σ
0.6	1488, 1323	1889, 1642
1.0	2981, 2629	3569, 3120
1.5	4354, 3840	5067, 4439
2.0	5568, 4916	6382, 5598
2.5	6712, 5931	7620, 6692
3.0	7805, 6898	8801, 7742
3.5	8868, 7838	9785, 8620
$m_h = 150[\text{GeV}]$	Λ_T [GeV]	
\sqrt{s}	<i>unpol.</i>	$J = 2$ <i>pol.</i>
[TeV]	3σ , 5σ	3σ , 5σ
0.6	1254, 1120	1500, 1306
1.0	2781, 2465	3256, 2848
1.5	4175, 3690	4766, 4179
2.0	5389, 4769	6074, 5336
2.5	6525, 5779	7288, 6416
3.0	7608, 6749	8458, 7450
3.5	8664, 7686	9600, 8458
$m_h = 200[\text{GeV}]$	Λ_T [GeV]	
\sqrt{s}	<i>unpol.</i>	$J = 2$ <i>pol.</i>
[TeV]	3σ , 5σ	3σ , 5σ
0.6	898, 798	1015, 885
1.0	2548, 2262	2971, 2596
1.5	3941, 3498	4495, 3953
2.0	5164, 4587	5827, 5135
2.5	6314, 5612	7061, 6235
3.0	7401, 6586	8236, 7280
3.5	8454, 7527	9375, 8288

Table 1: *The dependence of 3σ exclusion limits and 5σ observation limits on Λ_T and \sqrt{s} for the $\gamma\gamma \rightarrow t\bar{t}h^0$ process in both unpolarized and $P_\gamma=0.9$, $J=2$ polarized collision modes. The three tables correspond to $m_h = 115$, 150 and 200 GeV, respectively.*

In Figs.7(a), (b) and (c) we take $m_h = 115, 150$ and 200 GeV, separately. We can see that the relative value δ in $J=2$, $P_\gamma = 0.9$ polarized collision mode is much larger than in a unpolarized collision mode, especially in the case with large \sqrt{s} .

In Fig.8, we present the differential cross section $d\sigma/d\cos\theta$ of the process $\gamma\gamma \rightarrow t\bar{t}h^0$ as a function of $\cos\theta$, where the scattering angle θ is the angle between Higgs boson and one of the initial colliding photons. In Fig.8(a) the Higgs boson mass m_h , $\gamma\gamma$ colliding energy \sqrt{s} and Λ_T are fixed to be 115 GeV, 1 TeV and 2.5 TeV, respectively, and in Fig.8(b) the Higgs boson mass m_h , $\gamma\gamma$ colliding energy \sqrt{s} and Λ_T are fixed to be 115 GeV, 3 TeV and 5.5 TeV, respectively. As shown in these figures, the differential cross sections in the SM and LED model are the same in the $J = 0$ polarized $\gamma\gamma$ collision mode, and the line shapes for $J = 0$ and $J = 2$ polarized photon collisions are quite different. Fig.8(a) shows that for the $J = 0$ polarized $\gamma\gamma$ collision mode, the differential cross section is quite large when θ is in the vicinities of 0 or π . That means the outgoing Higgs bosons in the $J = 0$ polarized photon collision mode are almost collinear to the incoming photon beams. But in the case of $J = 2$, $\Lambda_T = 5.5$ TeV and $\sqrt{s} = 3$ TeV there is a large fraction of Higgs bosons emitting at large scattering angle ($\theta \sim \pi/2$) as shown in Fig.8(b).

In Fig.9, we show the differential cross section $d\sigma/dp_t$ of the process $\gamma\gamma \rightarrow t\bar{t}h^0$ as a function of the transverse momentum of the final Higgs boson p_t in the range of 0 to 1 TeV, with $m_h = 115$ GeV and $\sqrt{s} = 2$ TeV. As shown in this figure, the SM and LED model results for $J=0$ collision mode are the same (depicted as a dash-dotted curve), since the contribution of the virtual graviton exchange diagrams vanishes. We can see also that the effects of the large extra dimensions on differential cross

section $d\sigma/dp_t$ in a $J = 2$ polarized $\gamma\gamma$ collision mode is quantitatively enhanced comparing with that in unpolarized collision mode. Here we can conclude that the differential cross sections of $\gamma\gamma \rightarrow t\bar{t}h^0$ process in unpolarized and $J = 2$ polarized photon collision modes are sensitive to graviton exchanges, but there is no influence of the graviton exchange in the differential cross section of the $\gamma\gamma \rightarrow t\bar{t}h^0$ process with $J = 0$ polarizations of initial photons.

III.2 $e^+e^- \rightarrow t\bar{t}h^0$ process

For the process $e^+e^- \rightarrow t\bar{t}h^0$, we consider the collisions in the unpolarized and $++$, $+-$, $-+$ and $--$ polarized e^+e^- collision modes, the notation $+-$ represents the helicities of the initial positron and electron being $\lambda_1 = +1/2$ and $\lambda_2 = -1/2$, separately. In Fig.10, we present the cross section of $e^+e^- \rightarrow t\bar{t}h^0$ as a function of the c.m.s. energy \sqrt{s} with different kinds of polarizations of initial positron/electron. Here we take $m_h = 115 \text{ GeV}$ and $\Lambda_T = 3.5 \text{ TeV}$. Since the cross sections of the $++$ and $--$ polarized modes are too small, we only present the cross sections of unpolarized, $+-$ and $-+$ polarized e^+e^- collision modes. As showed in this figure, in the region of $\sqrt{s} < 1.5 \text{ TeV}$, the curves for LED model and SM merged together, but when $\sqrt{s} > 1.5 \text{ TeV}$, each of the three curves (solid, dashed and dotted curves) branches off into two curves. The lower one is for the σ_{SM} and the upper one is for the σ_{LED} . The figure shows that the $-+$ polarized e^+e^- collision to produce $t\bar{t}h^0$ would be the best channel in probing LED effects among all the $e^+e^- \rightarrow t\bar{t}h^0$ channels with other polarizations of initial particles, if the incoming positron and electron are completely polarized.

In Table.2, we present the relative discrepancy δ defined as in Eq.(3.6) for different polarization collision modes with some typical values of \sqrt{s} . Here we take $m_h = 115 \text{ GeV}$ and $\Lambda_T = 1.5 \text{ TeV}$, the polarization for positron is taken as $P_{e^+} = 0.6$ and for electron $P_{e^-} = 0.8$. We can see again the $-+$ polarized e^+e^- collision mode is the most significant one in probing the LED effects among all the polarization modes in the process $e^+e^- \rightarrow t\bar{t}h^0$. So in the following discussion, we compare the numerical results of process $e^+e^- \rightarrow t\bar{t}h^0$ in unpolarized collision mode only with that in the $-+$ polarized e^+e^- collision mode with $P_{e^+} = 0.6$ and $P_{e^-} = 0.8$.

\sqrt{s} [TeV]	δ		
	<i>unpol.</i>	<i>+ - pol.</i>	<i>- + pol.</i>
1	0.00236	0.00245	0.00470
2	0.72302	0.529594	1.15039
3	21.6655	15.9341	33.8929

Table 2: *The relative discrepancy δ in different collision modes for $e^+e^- \rightarrow t\bar{t}h^0$ process with some typical values of \sqrt{s} .*

Fig.11 exhibits the cross section of the process $e^+e^- \rightarrow t\bar{t}h^0$ in the SM and LED model as a function of \sqrt{s} , with different values of Λ_T and m_h . Figs.11(a), (c) and (e) are corresponding to the unpolarized photon collision mode and their results are coincident with those in Ref.[18]. From Figs.11(a), (c) and (e) we can get the the same conclusion as in Ref.[18] that in the unpolarized e^+e^- collision the virtual exchange KK gravitons can modify the cross section of process $e^+e^- \rightarrow t\bar{t}h^0$ significantly from its SM value. Figs.11(b), (d) and (f) are corresponding to the $-+$ polarized e^+e^- collision mode with $P_{e^+} = 0.6$ and $P_{e^-} = 0.8$. Analogous to the process $\gamma\gamma \rightarrow t\bar{t}h^0$, when \sqrt{s} is large enough, the LED cross sections increase while

the SM ones decrease with the increment of \sqrt{s} . We find that in case of taking the same values of \sqrt{s} , m_h and Λ_T , within the framework of the LED model in $-+$ polarized e^+e^- collision mode with $P_{e^+} = 0.6$ and $P_{e^-} = 0.8$, the cross section is larger than that in unpolarized e^+e^- collision, but the SM cross section remains the same in both two kinds of polarizations.

In Fig.12, we present the cross section of the process $e^+e^- \rightarrow t\bar{t}h^0$ as a function of Λ_T with different values of \sqrt{s} and m_h . Figs.12(a),(c) and (e) are for unpolarized e^+e^- collision with $m_h = 115 \text{ GeV}$, $m_h = 150 \text{ GeV}$ and $m_h = 200 \text{ GeV}$, respectively. Figs.12(b), (d) and (f) are for $-+$, $P_{e^-} = 0.8$ and $P_{e^-} = 0.6$ polarized e^+e^- collision, with $m_h = 115 \text{ GeV}$, $m_h = 150 \text{ GeV}$ and $m_h = 200 \text{ GeV}$, separately. The solid, dashed and dotted curves are corresponding to $\sqrt{s} = 1, 2, 3 \text{ TeV}$, respectively. The upper curves are the LED results while the lower straight lines are the corresponding SM results. As we expect, all the LED results decrease to their corresponding SM results as the increment of Λ_T .

In Fig.13, we show the regions in the $\sqrt{s} - \Lambda_T$ parameter space, where the LED effect can and cannot be observed from process $e^+e^- \rightarrow t\bar{t}h^0$ in unpolarized photon collision mode according to the criteria shown in Eq.(3.4) and Eq.(3.5). Figs.13(a), (b) and (c) correspond to $m_h = 115, 150$ and 200 GeV , respectively. Here we assume the LC integrated luminosity $\mathcal{L} = \mathcal{L}_{e^+e^-} = 500 \text{ fb}^{-1}$. The underside region is excluded by the unitarity bounds.

In Table 3, we present the 3σ exclusion limits and corresponding 5σ observation limits for the $e^+e^- \rightarrow t\bar{t}h^0$ process with $m_h = 115, 150, 200 \text{ GeV}$ and some typical values of \sqrt{s} . Both unpolarized and $-+$, $P_{e^+} = 0.6$, $P_{e^-} = 0.8$ polarized e^+e^-

$m_h = 115[\text{GeV}]$	Λ_T [GeV]	
\sqrt{s}	<i>unpol.</i>	$- +$ <i>pol.</i>
[TeV]	3σ , 5σ	3σ , 5σ
0.6	1114, 1042	1183, 1105
1.0	2135, 1988	2264, 2105
1.5	3233, 3003	3416, 3173
2.0	4275, 3963	4515, 4188
2.5	5287, 4903	5577, 5169
3.0	6268, 5815	6614, 6125
3.5	7235, 6703	7629, 7061
$m_h = 150[\text{GeV}]$	Λ_T [GeV]	
\sqrt{s}	<i>unpol.</i>	$- +$ <i>pol.</i>
[TeV]	3σ , 5σ	3σ , 5σ
0.6	999, 933	1059, 988
1.0	2058, 1919	2179, 2029
1.5	3176, 2953	3356, 3117
2.0	4229, 3927	4463, 4139
2.5	5246, 4867	5531, 5128
3.0	6241, 5782	6573, 6089
3.5	7205, 6672	7589, 7026
$m_h = 200[\text{GeV}]$	Λ_T [GeV]	
\sqrt{s}	<i>unpol.</i>	$- +$ <i>pol.</i>
[TeV]	3σ , 5σ	3σ , 5σ
0.6	787, 728	833, 770
1.0	1964, 1830	2079, 1936
1.5	3111, 2893	3285, 3054
2.0	4186, 3888	4413, 4098
2.5	5215, 4838	5498, 5095
3.0	6212, 5757	6542, 6061
3.5	7192, 6657	7566, 7003

Table 3: *The dependence of 3σ exclusion limits and corresponding 5σ observation limits on Λ_T and \sqrt{s} for the $e^+e^- \rightarrow t\bar{t}h^0$ process. The three tables are corresponding to $m_h=115$, 150 and 200 GeV, respectively. For the $-+$ polarized e^+e^- collision mode, we set $P_{e^+} = 0.6$ and $P_{e^-} = 0.8$.*

collision modes are considered. From this table we can find that by using the process $e^+e^- \rightarrow t\bar{t}h^0$ in the $-+$ polarized e^+e^- collision mode, the sensitivity to the observation LED effects is improved a little comparing with that by using the unpolarized collision e^+e^- mode.

IV summary

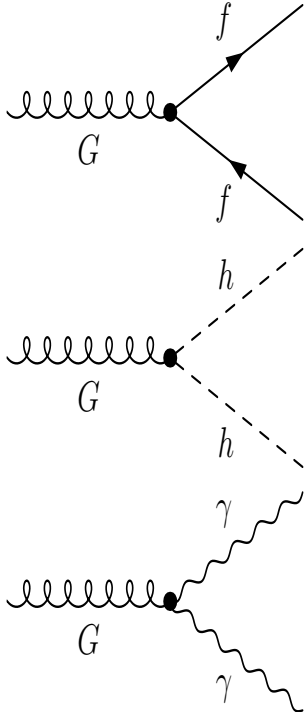
In this paper, we studied the LED effects in both the $\gamma\gamma \rightarrow t\bar{t}h^0$ and $e^+e^- \rightarrow t\bar{t}h^0$ processes at future linear colliders. We conclude that the virtual Kaluza-Klein (KK) graviton exchange can modify significantly both the $\sigma(\gamma\gamma \rightarrow t\bar{t}h^0)$ and $\sigma(e^+e^- \rightarrow t\bar{t}h^0)$ for some polarizations of initial photons from their corresponding SM values. Our numerical results show that when we take $m_h = 115$ GeV and $\sqrt{s} = 3.5$ TeV, the effective scale Λ_T for the process $\gamma\gamma \rightarrow t\bar{t}h^0$ can be probed up to 7.8 and 8.6 TeV in the unpolarized and $P_\gamma = 0.9$, $J=2$ polarized $\gamma\gamma$ collision modes separately, while for the $e^+e^- \rightarrow t\bar{t}h^0$ process the upper limits of Λ_T to observe the LED effects are 6.7 TeV and 7.0 TeV in the unpolarized and $P_{e^+} = 0.6$, $P_{e^-} = 0.8$, $-+$ polarized e^+e^- collision modes, respectively. Therefore, the sensitivity in probing LED effects can be significantly improved by using the $\gamma\gamma \rightarrow t\bar{t}h^0$ process with $J=2$ polarizations of colliding photons. We find that the differential cross sections of $\gamma\gamma \rightarrow t\bar{t}h^0$ process in unpolarized and $J = 2$ polarized photon collision modes are sensitive to graviton exchanges too, but there is no influence of the graviton exchange on the differential cross section of the $\gamma\gamma \rightarrow t\bar{t}h^0$ process with $J = 0$ polarizations of initial photons. We also find that in the case of $e^+e^- \rightarrow t\bar{t}h^0$ process with $-+$ polarization of e^+e^- colliding beams, the upper limit of Λ_T to be probed is

not obviously improved. Comparing all the $t\bar{t}h^0$ associated production channels at linear colliders with different polarizations of initial photons(or positron/electron), we find the process $\gamma\gamma \rightarrow t\bar{t}h^0$ with $J = 2$ polarizations of initial photons provides a possibility to improve significantly the sensitivity in probing the LED effects.

Acknowledgments: This work was supported in part by the National Natural Science Foundation of China and a special fund sponsored by China Academy of Science.

V Appendix

In this Appendix, we present the explicit expressions of the Feynman rules which are relevant to our calculation of the processes $\gamma\gamma \rightarrow t\bar{t}h^0$ and $e^+e^- \rightarrow t\bar{t}h^0$.



$$C_{ffG} : -i\frac{\kappa}{8\sqrt{V_n}} [\gamma_\mu(p_1 + p_2)_\nu + \gamma_\nu(p_1 + p_2)_\mu - 2g_{\mu\nu}(\not{p}_1 + \not{p}_2 - 2m_f)]$$

$$C_{hhG} : i\frac{\kappa}{\sqrt{V_n}} [B_{\mu\nu\alpha\beta}p_1^\alpha p_2^\beta - A_{\mu\nu}m_h^2]$$

$$C_{\gamma\gamma G} : i\frac{\kappa}{\sqrt{V_n}} (C_{\mu\nu\alpha\beta\rho\sigma} - C_{\mu\nu\alpha\sigma\beta\rho})k_1^\rho k_2^\sigma \delta^{ab}$$

where

$$\begin{aligned}
A^{\mu\nu} &= \frac{1}{2}g^{\mu\nu}, \\
B^{\mu\nu\alpha\beta} &= \frac{1}{2}(g^{\mu\nu}g^{\alpha\beta} - g^{\mu\alpha}g^{\nu\beta} - g^{\mu\beta}g^{\nu\alpha}), \\
C^{\rho\sigma\mu\nu\alpha\beta} &= \frac{1}{2}[g^{\rho\sigma}g^{\mu\nu}g^{\alpha\beta} - (g^{\rho\mu}g^{\sigma\nu}g^{\alpha\beta} + g^{\rho\nu}g^{\sigma\mu}g^{\alpha\beta} + g^{\rho\alpha}g^{\sigma\beta}g^{\mu\nu} + g^{\rho\beta}g^{\sigma\alpha}g^{\mu\nu})], \\
\frac{\kappa}{\sqrt{V_n}} &= \frac{4\sqrt{\pi}}{M_{pl}},
\end{aligned} \tag{5.1}$$

and $(g_{\mu\nu}) = \text{diag}\{1, -1, -1, -1\}$ is the metric tensor of the 4-dimensional flat space-time manifold.

References

- [1] Nima Arkani-Hamed, Savas Dimopoulos, Gia Dvali, Phys. Lett. **B429** (1998) 263-272; Nima Arkani-Hamed, Savas Dimopoulos, Gia Dvali, Phys. Rev. **D59** (1999) 086004; I. Antoniadis, N. Arkani-Hamed, S. Dimopoulos, G. Dvali, Phys. Lett. **B436** (1998) 257-263.
- [2] Lisa Randall, Raman Sundrum, Phys. Rev. Lett. **83** (1999) 3370-3373; Lisa Randall, Raman Sundrum, Phys. Rev. Lett. **83** (1999) 4690.
- [3] H. P. Nilles Phys. Rep. **110** (1984) 1; H. E. Haber and G. L. Kane, Phys. Rep. **117** (1985) 75; J. F. Gunion and H. E. Haber, Nucl. Phys. **B272** (1986) 1.
- [4] S. Weinberg, Phys. Rev. **D19** (1979) 1277; L. Susskind, Phys. Rev. **D20** (1979) 2619; S. Dimopoulos and L. Susskind, Nucl. Phys. **B155** (1979) 237; E. Eichten and K. Lane, Phys. Lett. **B90** (1980) 125.

- [5] C. D. Hoyle, U. Schmidt, B. R. Heckel, E. G. Adelberger, J. H. Gundlach, D. J. Kapner, H. E. Swanson, Phys. Rev. Lett. **86** (2001) 1418-1421.
- [6] S. Cullen, M. Perelstein, Phys. Rev. Lett. **83** (1999) 268-271; L. Hall, D. Smith, Phys. Rev. **D60** (1999) 085008 .
- [7] JoAnne L. Hewett, Phys. Rev. Lett. **82** (1999) 4765-4768.
- [8] D0 Collaboration, Phys. Rev. Lett. **86** (2001) 1156-1161.
- [9] Michiel Sanders, for the CDF, D0 collaborations, hep-ex/0310033, To be published in proceedings of the International Europhysics Conference on High Energy Physics, Aachen, Germany, July 2003, Eur. Phys. J. **C33**, s770-s772 (2004).
- [10] Laurent Vacavant, for the ATLAS Collaboration, the CMS Collaboration, hep-ex/0310020, Proceedings of the International Europhysics Conference on High Energy Physics EPS 2003 (July 17-23, 2003), Aachen, Germany, Eur. Phys. J. **C33** (2004) S924-S926.
- [11] ZEUS Collaboration, Phys.Lett. **B591** (2004) 23-41, arXiv:hep-ex/0401009.
- [12] J. Hewett and M. Spiropulu, Ann. Rev. Nucl. Part. Sci. **52** (2002) 397-424.
- [13] G. Landsberg, To appear in Proceedings of SLAC Summer Institute, 2004. An extended version of the talk given on behalf of the CDF and D0 Collaborations.
- [14] Tao Han, Joseph D. Lykken, Ren-Jie Zhang, Phys. Rev. **D59** (1999) 105006.

- [15] Gian F. Giudice, Riccardo Rattazzi, James D. Wells, Nucl.Phys. **B544** (1999) 3-38.
- [16] Thomas G. Rizzo, Phys. Rev. **D60** (1999) 115010.
- [17] Anindya Datta, Emidio Gabrielli, Barbara Mele, JHEP **0310** (2003) 003.
- [18] D. Choudhury, N. G. Deshpande, D. K. Ghosh, JHEP **0409** (2004) 055, arXiv:hep-ph/0311284.
- [19] N.G. Deshpande and D.K. Ghosh, Phys. Rev. **D67** (2003) 113006, arXiv:hep-ph/0301272.
- [20] I.F. Ginzburg, G.L. Kotkin, V.G. Serbo and V.I. Telov, Nucl. Instrum. Meth. Nucl. Instrum. Meth. **A205**, 47(1983); I.F. Ginzburg, G.L. Kotkin, V.G. Panfil, V.G. Serbo and V.I. Telov, Nucl. Instrum. Meth. **A219**, 5(1984).
- [21] Chen Hui, Ma Wen-Gan, Zhang Ren-You, Zhou Pei-Jun, Hou Hong-Sheng and Sun yan-Bin, Nucl. Phys. **B683** (2004) 196-218, arXiv:hep-ph/0309106.
- [22] Aurelio Juste, Gonzalo Merino, hep-ph/9910301.
- [23] T. Abe, et al. [American Linear Collider Working Group Collaboration], Linear collider physics resource book for Snowmass 2001, in Proc. of the APS/DPF/DPB Summer Study on the Future of Particle Physics (Snowmass 2001) arXiv:hep-ex/0106055, arXiv:hep-ex/0106056, arXiv:hep-ex/0106057, arXiv:hep-ex/0106058, and the references therein.
- [24] H. Baer, S. Dawson and L. Reina, Phys. Rev. **D61** (2000) 013002.

- [25] S. Dittmaier, M. Krämer, Y. Liao, M. Spira, P.M. Zerwas, Phys. Lett. **B478** (2000) 247-254.
- [26] You Yu, Ma Wen-Gan, Chen Hui, Zhang Ren-You, Sun Yan-Bin, Hou Hong-Sheng, Phys. Lett. **B571**(2003) 85-91, hep-ph/0306036; G. Belanger, F. Boudjema, J. Fujimoto, T. Ishikawa, T. Kaneko, K. Kato, Y. Shimizu, Y. Yasui, Phys. Lett. **B571** (2003) 163-172, hep-ph/0307029; A. Denner, S. Dittmaier, M. Roth, M.M. Weber, Phys. Lett. **B575** (2003) 290-299, arXiv:hep-ph/0307193.
- [27] Kingman Cheung, Phys. Rev. **D47** (1993) 3750-3756, arXiv:hep-ph/9211262.
- [28] S. Eidelman, *et al.*, Phys. Lett. **B592**(2004)1.
- [29] Koya Abe, etal., 'GLC Project, Linear Collider for TeV Physics', KEK Report 2003-7, September 2003, A/H.

Figure Captions

Fig.1 The tree-level Feynman diagrams with graviton exchange for the process $\gamma\gamma \rightarrow t\bar{t}h^0$.

Fig.2 The tree-level Feynman diagrams with graviton exchange for the process $e^+e^- \rightarrow t\bar{t}h^0$.

Fig.3 (a) The cross section for the process $\gamma\gamma \rightarrow t\bar{t}h^0$ as a function of the c.m.s.energy for different kinds of collision modes. (b) The cross sections/ratio of σ_{+-} and σ_{++} as the functions of \sqrt{s} .

Fig.4 The dependence of the cross section for $\gamma\gamma \rightarrow t\bar{t}h^0$ on \sqrt{s} . (a),(c) and (e) are for unpolarized photon collisions with $m_h = 115 \text{ GeV}$, $m_h = 150 \text{ GeV}$ and $m_h = 200 \text{ GeV}$, respectively. (b), (d) and (f) are for $+-$, $P_\gamma = 0.9$ polarized photon collisions with $m_h = 115 \text{ GeV}$, $m_h = 150 \text{ GeV}$ and $m_h = 200 \text{ GeV}$, respectively.

Fig.5 The dependence of the cross section for $\gamma\gamma \rightarrow t\bar{t}h^0$ on effective scale Λ_T . (a),(c) and (e) are for unpolarized photon collisions with $m_h = 115 \text{ GeV}$, $m_h = 150 \text{ GeV}$ and $m_h = 200 \text{ GeV}$, respectively. (b), (d) and (f) are for $+-$, $P_\gamma = 0.9$ polarized photon collisions with $m_h = 115 \text{ GeV}$, $m_h = 150 \text{ GeV}$ and $m_h = 200 \text{ GeV}$, respectively.

Fig.6 The LED effect observation area (gray) and the LED effect exclusion area (pale gray) for $\gamma\gamma \rightarrow t\bar{t}h^0$ process in the $\sqrt{s} - \Lambda_T$ parameter space considering only unpolarized beams with $m_h = 115, 150$ and 200 GeV , respectively.

Fig.7 The δ dependence of the process $\gamma\gamma \rightarrow t\bar{t}h^0$ with unpolarized and $J = 2$, $P_\gamma = 0.9$ polarized photon collisions on \sqrt{s} . (a),(b) and (c) are for $m_h = 115 \text{ GeV}$, $m_h = 150 \text{ GeV}$ and $m_h = 200 \text{ GeV}$, respectively.

Fig.8 The differential cross section $d\sigma/d\cos\theta$ of the process $\gamma\gamma \rightarrow t\bar{t}h^0$ as a function of $\cos\theta$ in different polarization collision modes (unpolarized, $J = 0$ and $J = 2$ polarized $\gamma\gamma$ collision modes) within both the SM and LED model.

Fig.9 The differential cross section $d\sigma/dp_t$ of the process $\gamma\gamma \rightarrow t\bar{t}h^0$ as a function of the transverse momentum of the final Higgs boson p_t in different collision modes (unpolarized, $J = 0$ and $J = 2$ polarized $\gamma\gamma$ collision modes) within both the SM and LED model.

Fig.10 The cross section of the process $e^+e^- \rightarrow t\bar{t}h^0$ as a function of the c.m.s. energy \sqrt{s} in unpolarized, $+-$ and $-+$ polarized e^+e^- collision modes, when $m_h=115\text{GeV}$, $\Lambda_T=3.5\text{ TeV}$.

Fig.11 The dependence of the cross section for $e^+e^- \rightarrow t\bar{t}h^0$ on \sqrt{s} . (a),(c) and (e) are for unpolarized e^+e^- collision with $m_h = 115\text{ GeV}$, $m_h = 150\text{ GeV}$ and $m_h = 200\text{ GeV}$, respectively. (b), (d) and (f) are for $-+$, $P_{e^+} = 0.6$ and $P_{e^-} = 0.8$ polarized e^+e^- collision with $m_h = 115\text{ GeV}$, $m_h = 150\text{ GeV}$ and $m_h = 200\text{ GeV}$, respectively.

Fig.12 The dependence of the cross section for $e^+e^- \rightarrow t\bar{t}h^0$ on Λ_T . (a),(c) and (e) are for unpolarized e^+e^- collision with $m_h = 115\text{ GeV}$, $m_h = 150\text{ GeV}$ and $m_h = 200\text{ GeV}$, respectively. (b), (d) and (f) are for $-+$, $P_{e^+} = 0.6$ and $P_{e^-} = 0.8$ polarized e^+e^- collision with $m_h = 115\text{ GeV}$, $m_h = 150\text{ GeV}$ and $m_h = 200\text{ GeV}$,

respectively.

Fig.13 The LED effect observation area (gray) and the LED effect exclusion area (pale gray) for $e^+e^- \rightarrow t\bar{t}h^0$ process in unpolarized e^+e^- collision mode in the $\sqrt{s} - \Lambda_T$ parameter space. Fig.13(a), (b) and (c) are for $m_h = 115, 150$ and 200 GeV, respectively.

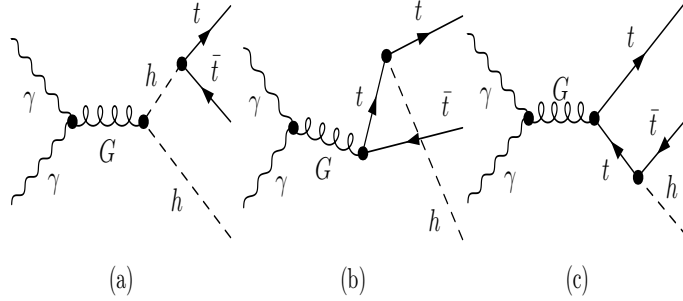


Figure 1: The tree-level Feynman diagrams with graviton exchange for the process $\gamma\gamma \rightarrow t\bar{t}h^0$.

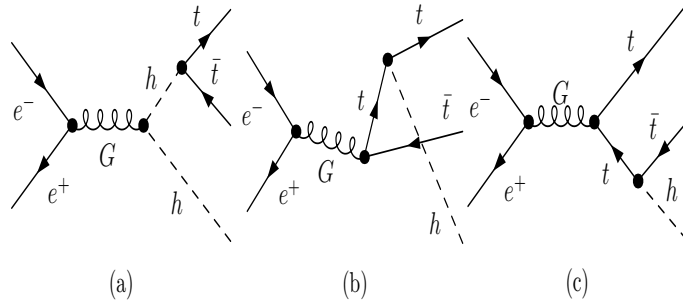


Figure 2: The tree-level Feynman diagrams with graviton exchange for the process $e^+e^- \rightarrow t\bar{t}h^0$.

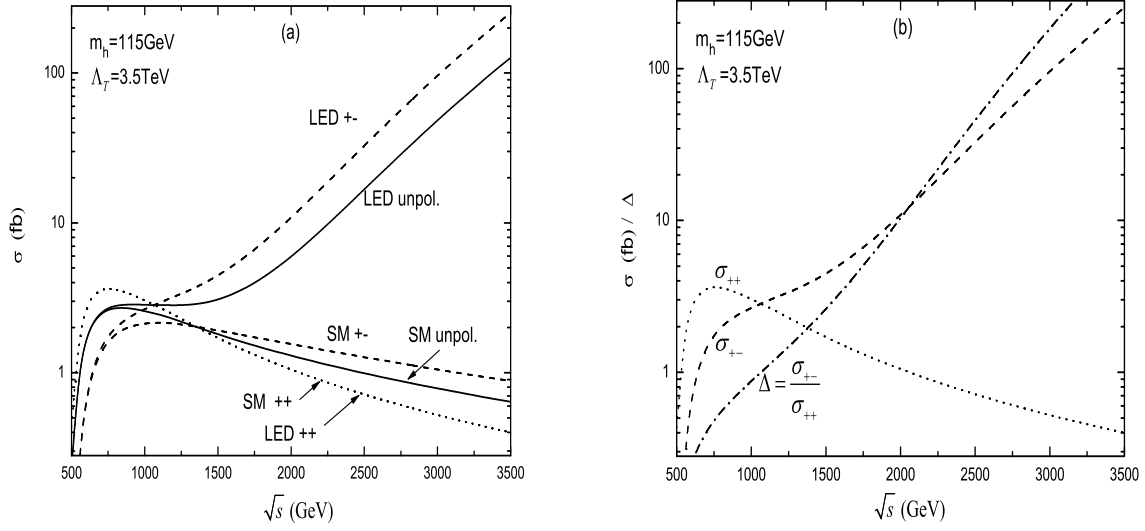


Figure 3: (a) The cross section for the process $\gamma\gamma \rightarrow t\bar{t}h^0$ as a function of the c.m.s. energy for different kinds of collision modes. (b) The cross sections/ratio of σ_{+-} and σ_{++} as the functions of \sqrt{s} .

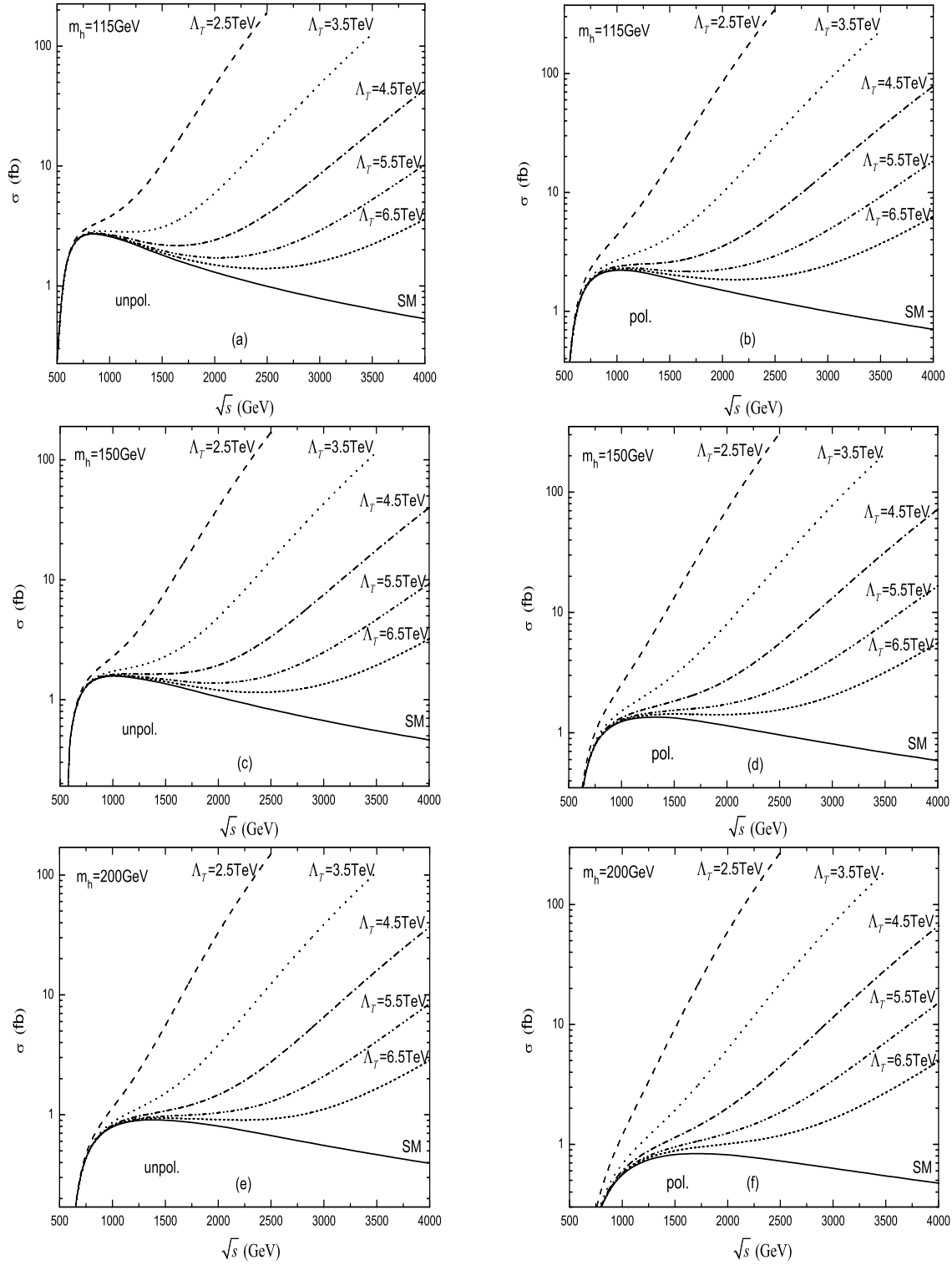


Figure 4: The dependence of the cross section for $\gamma\gamma \rightarrow t\bar{t}h^0$ on \sqrt{s} . (a),(c) and (e) are for unpolarized photon collisions with $m_h = 115$ GeV, $m_h = 150$ GeV and $m_h = 200$ GeV, respectively. (b), (d) and (f) are for $+-$, $P_\gamma = 0.9$ polarized photon collisions with $m_h = 115$ GeV, $m_h = 150$ GeV and $m_h = 200$ GeV, respectively.

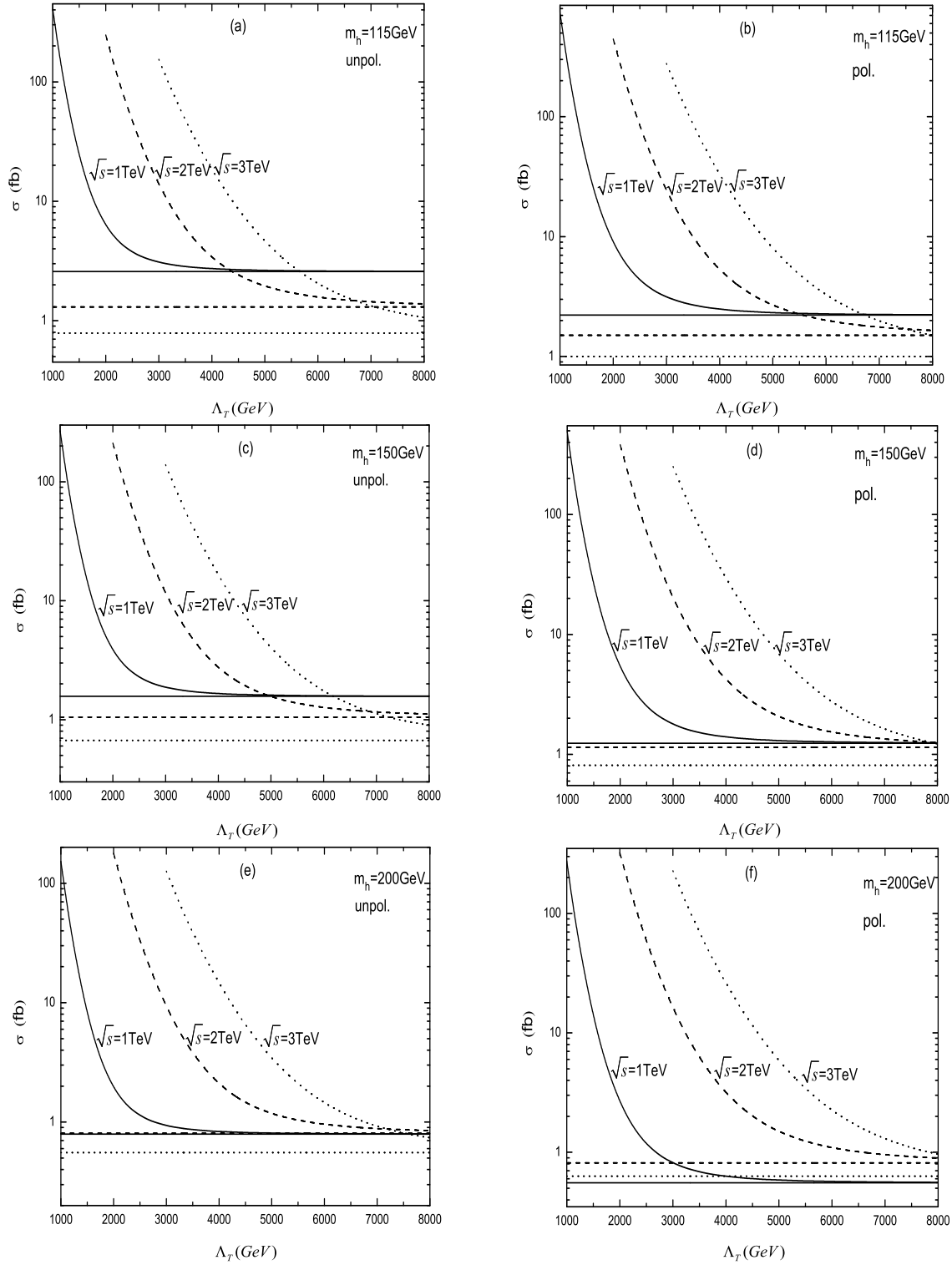


Figure 5: The dependence of the cross section for $\gamma\gamma \rightarrow t\bar{t}h^0$ on effective scale Λ_T . (a), (c) and (e) are for unpolarized photon collisions with $m_h = 115$ GeV, $m_h = 150$ GeV and $m_h = 200$ GeV, respectively. (b), (d) and (f) are for $+-$, $P_\gamma = 0.9$ polarized photon collisions with $m_h = 115$ GeV, $m_h = 150$ GeV and $m_h = 200$ GeV, respectively.

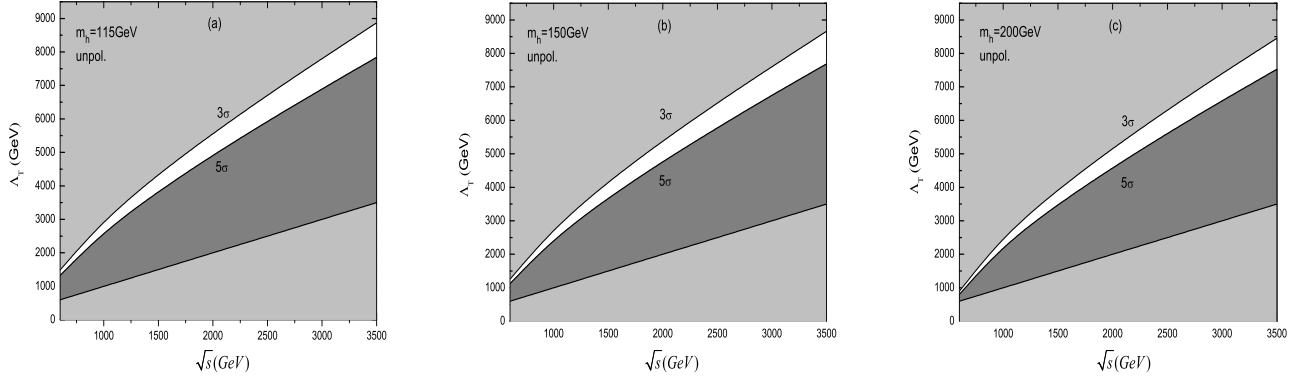


Figure 6: The LED effect observation area (gray) and the LED effect exclusion area (pale gray) for $\gamma\gamma \rightarrow t\bar{t}h^0$ process in the $\sqrt{s} - \Lambda_T$ parameter space considering only unpolarized beams with $m_h = 115, 150$ and 200 GeV, respectively.

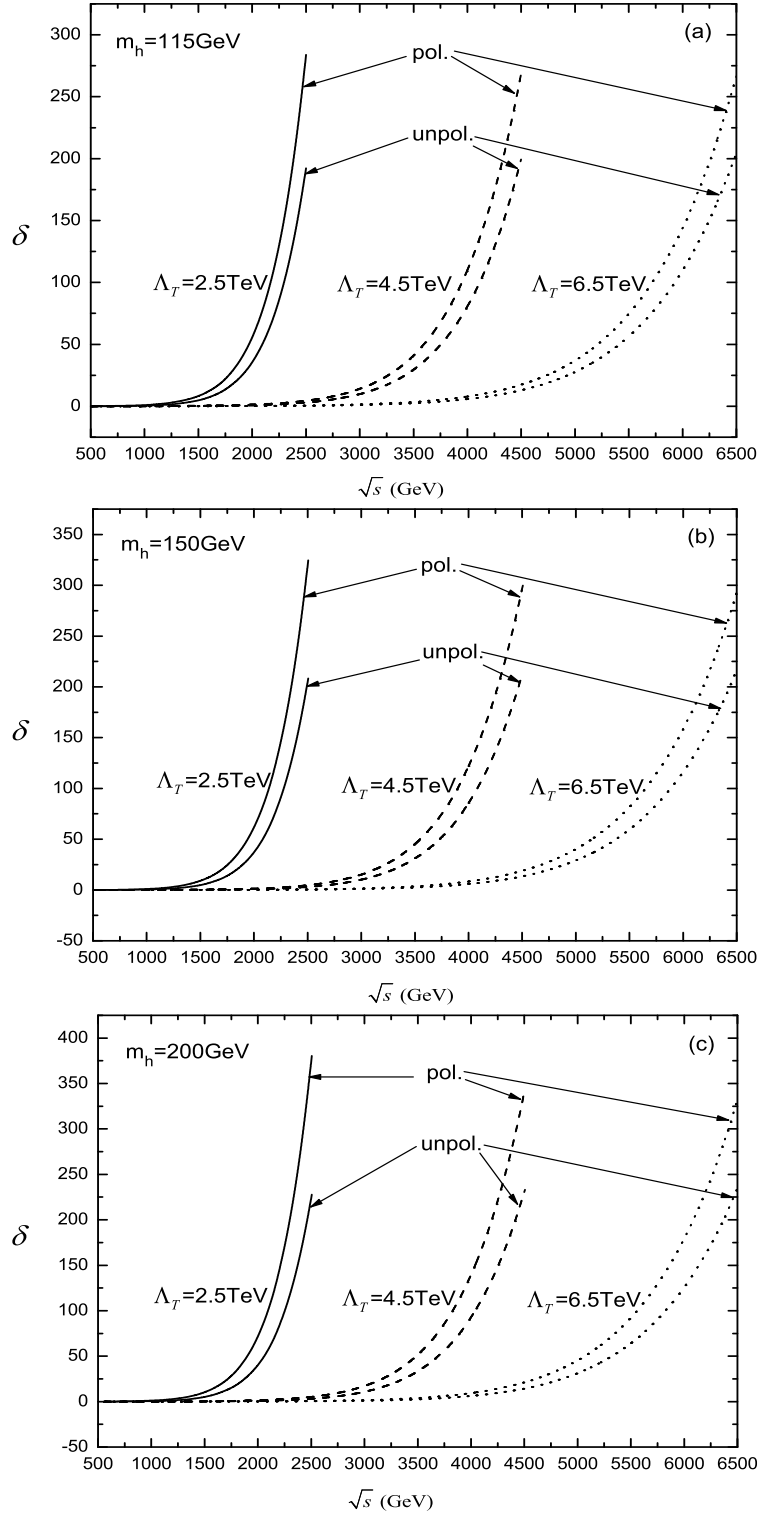


Figure 7: The δ dependence of the process $\gamma\gamma \rightarrow t\bar{t}h^0$ with unpolarized and $J = 2$, $P_\gamma = 0.9$ polarized photon collisions on \sqrt{s} . (a), (b) and (c) are for $m_h = 115$ GeV, $m_h = 150$ GeV and $m_h = 200$ GeV, respectively.

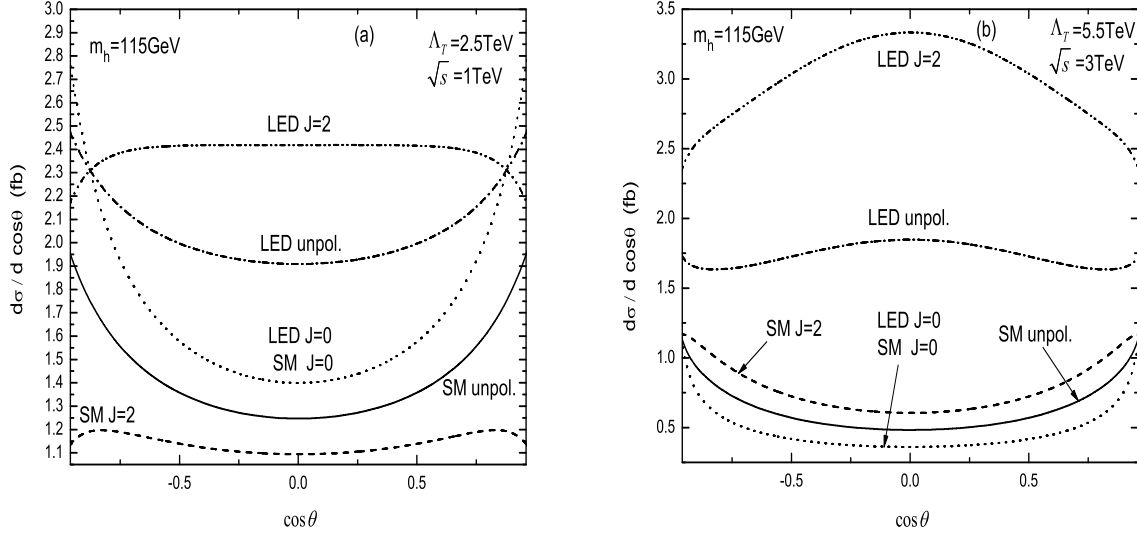


Figure 8: The differential cross section $d\sigma/d\cos\theta$ of the process $\gamma\gamma \rightarrow t\bar{t}h^0$ as a function of $\cos\theta$ in different polarization collision modes (unpolarized, $J = 0$ and $J = 2$ polarized $\gamma\gamma$ collision modes) within both the SM and LED model.

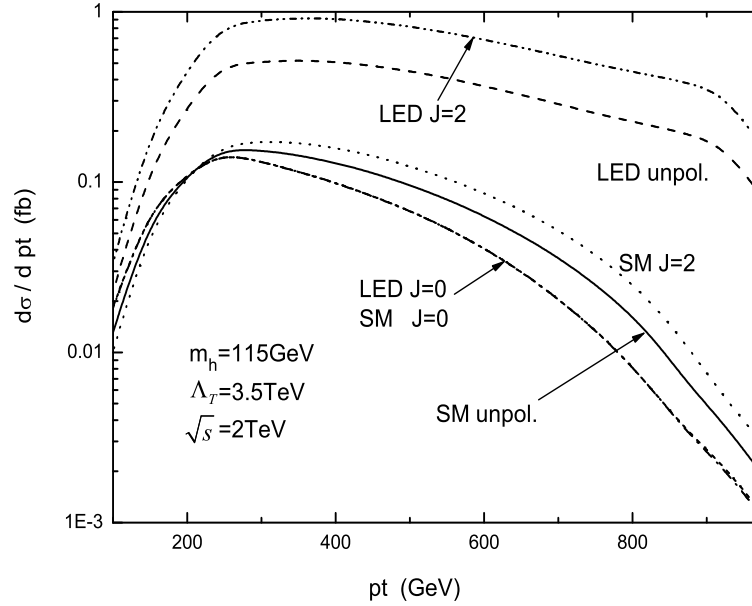


Figure 9: The differential cross section $d\sigma/dp_t$ of the process $\gamma\gamma \rightarrow t\bar{t}h^0$ as a function of the transverse momentum of the final Higgs boson p_t in different collision modes (unpolarized, $J = 0$ and $J = 2$ polarized $\gamma\gamma$ collision modes) within both the SM and LED model.

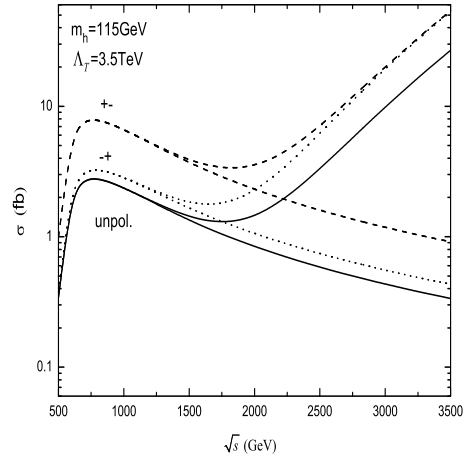


Figure 10: *The cross section of the process $e^+e^- \rightarrow t\bar{t}h^0$ as a function of the c.m.s. energy \sqrt{s} in unpolarized, $+-$ and $-+$ polarized e^+e^- collision modes, when $m_h=115\text{GeV}$, $\Lambda_T=3.5\text{ TeV}$.*

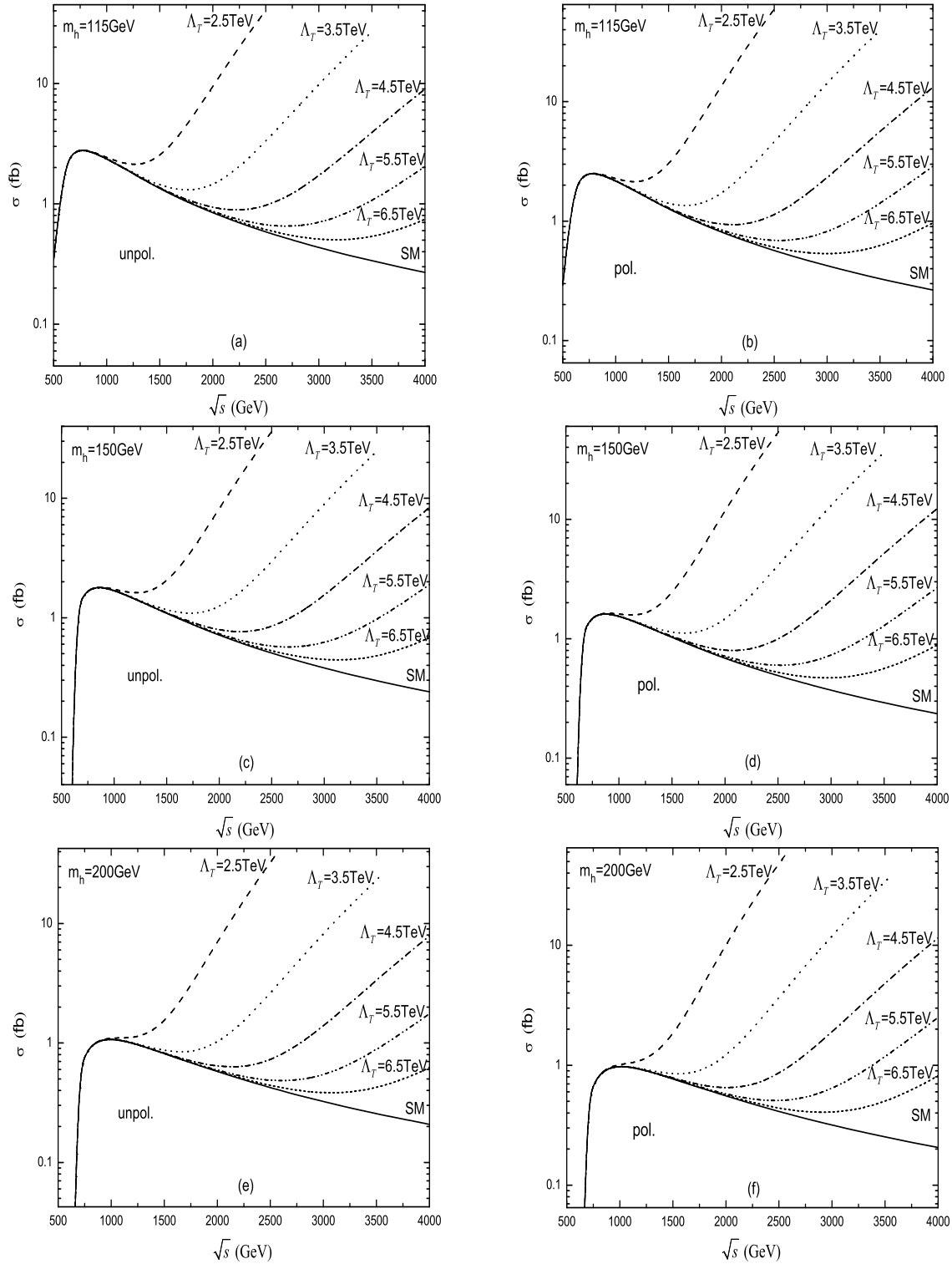


Figure 11: *The dependence of the cross section for $e^+e^- \rightarrow t\bar{t}h^0$ on \sqrt{s} . (a),(c) and (e) are for unpolarized e^+e^- collision with $m_h = 115$ GeV, $m_h = 150$ GeV and $m_h = 200$ GeV, respectively. (b), (d) and (f) are for $-, +$, $P_{e^+} = 0.6$ and $P_{e^-} = 0.8$ polarized e^+e^- collision with $m_h = 115$ GeV, $m_h = 150$ GeV and $m_h = 200$ GeV, respectively.*

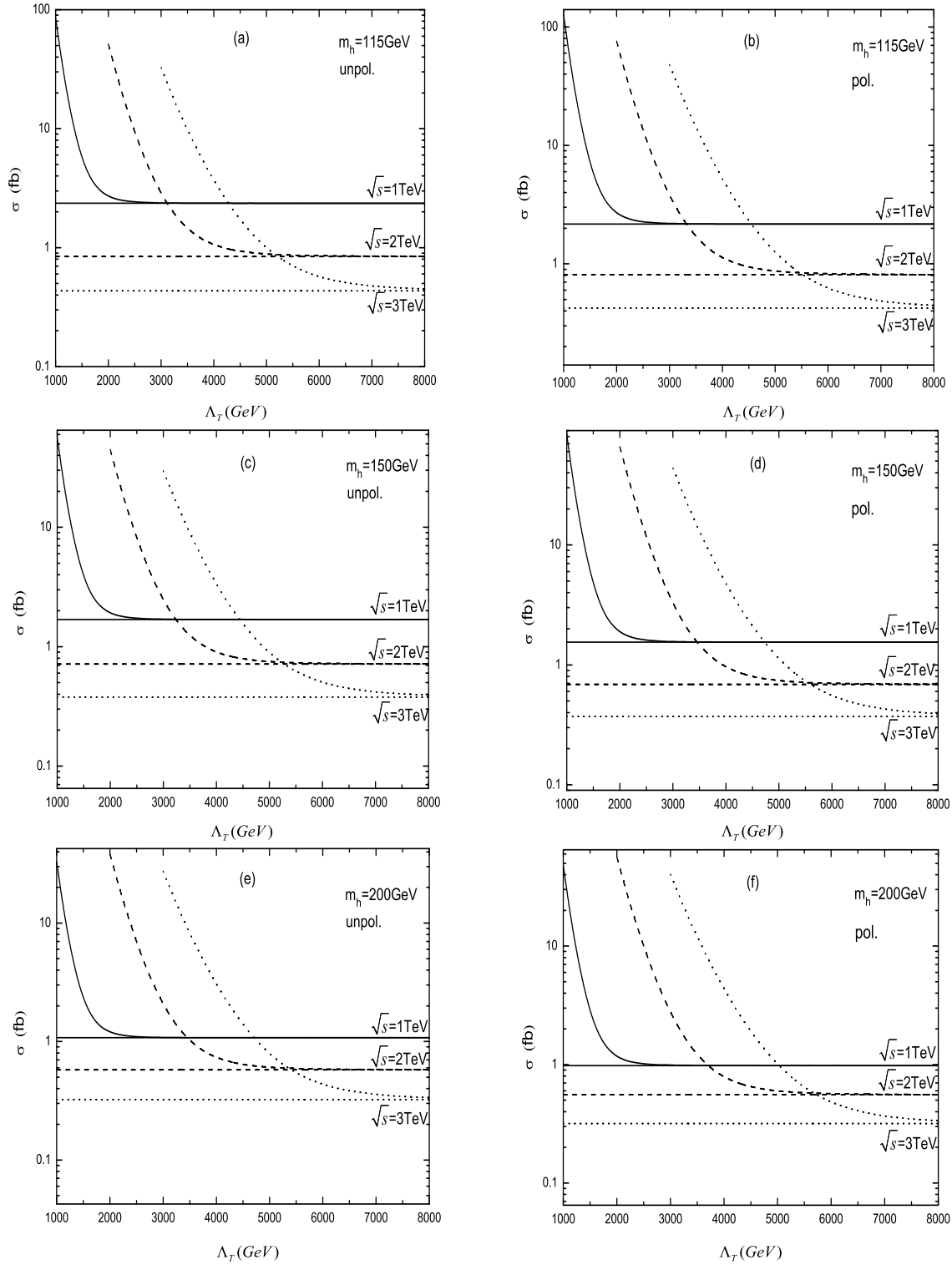


Figure 12: The dependence of the cross section for $e^+e^- \rightarrow t\bar{t}h^0$ on Λ_T . (a),(c) and (e) are for unpolarized e^+e^- collision with $m_h = 115$ GeV, $m_h = 150$ GeV and $m_h = 200$ GeV, respectively. (b), (d) and (f) are for $-, +, P_{e^+} = 0.6$ and $P_{e^-} = 0.8$ polarized e^+e^- collision with $m_h = 115$ GeV, $m_h = 150$ GeV and $m_h = 200$ GeV, respectively.

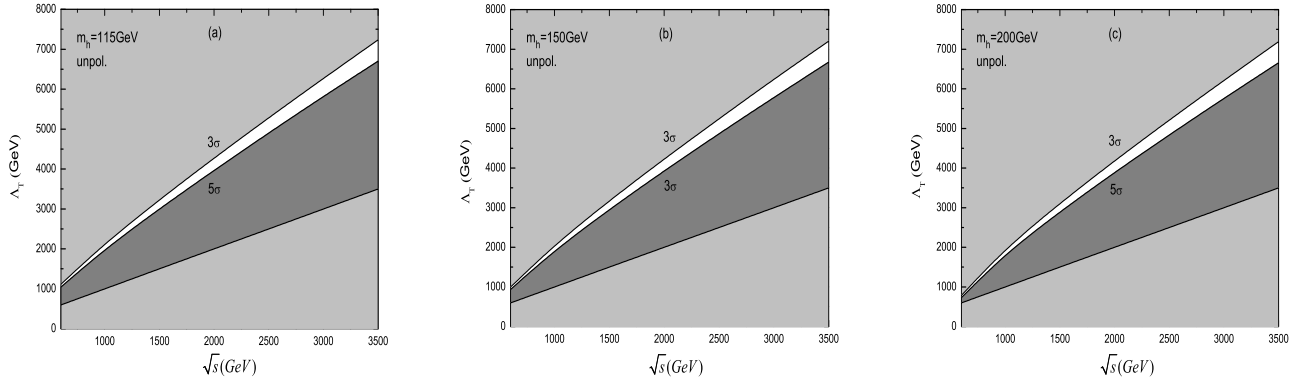


Figure 13: The LED effect observation area (gray) and the LED effect exclusion area (pale gray) for $e^+e^- \rightarrow t\bar{t}h^0$ process in unpolarized e^+e^- collision mode in the $\sqrt{s} - \Lambda_T$ parameter space. Fig.13(a), (b) and (c) are for $m_h = 115, 150$ and 200 GeV, respectively.